

PHYSICAL METALLURGY
AND HEAT TREATMENT

Comparative Study of Coatings formed by Electrospark Alloying Using TiC–NiCr and TiC–NiCr–Eu₂O₃ Electrodes

Ph. V. Kiryukhantsev-Korneev^{a, *}, A. D. Sytchenko^{a, **}, and E. A. Levashov^{a, ***}

^aNational University of Science and Technology “MISIS”, Moscow, 119049 Russia

*e-mail: kiruhancev-korneev@yandex.ru

**e-mail: alina-sytchenko@yandex.ru

***e-mail: levashov@shs.misis.ru

Received May 24, 2019; revised June 25, 2019; accepted June 27, 2019

Abstract—Coatings formed on steel 40Kh by electrospark alloying (ESA) using TiC–NiCr and TiC–NiCr–Eu₂O₃ electrodes are investigated. The coatings are deposited using an Alier-Metal 303 installation in argon under a normal pressure in the direct and opposite polarity modes. The structure, elemental composition, and phase composition of electrodes and coatings are investigated using X-ray phase analysis, scanning electron microscopy, energy dispersion spectroscopy, glow discharge optical emission spectroscopy, and optical profilometry. Mechanical and tribological properties of coatings are determined by nanoindentation and testing according to the “pin–disc” scheme, including elevated temperature in a range of 20–500°C. The tests for abrasive wear are performed using a Calowear tester, the impact resistance is studied using a CemeCon impact tester, and gas and electrochemical corrosion resistance are studied. The results show that the electrodes contain titanium carbide, the solid solution of nickel in chromium, and europium oxide in the case of a doped sample. Coating also included these phases, but the solid solution is formed based on iron. Coatings with the Eu₂O₃ additive are not substantially different in regards to structural characteristics, hardness, and friction coefficient, but exceed base coatings by abrasive resistance, cyclic impact resistance, and heat and corrosion resistance. An increase in impact resistance by a factor of 1.2–2.0, a decrease in the corrosion current more than 20-fold, and an almost twofold decrease in the oxidation index are observed upon the passage to doped coatings.

Keywords: electrospark deposition, TiC–NiCr, europium oxide, coatings, mechanical and tribological properties, abrasive wear resistance, impact resistance

DOI: 10.3103/S1067821219060099

INTRODUCTION

One important problem of modern production is the wear of parts and metallic constructions during the operation. To increase wear resistance and service life, it is sufficient to modify only the surface of wares by the deposition of protective coatings. One promising deposition method is electrospark alloying (ESA), which has substantial advantages such as high adhesion, the possibility of local surface treatment, a low thermal effect on the substrate, and the absence of severe requirements for surface preparation before the deposition [1, 2].

The development of materials based on tungsten-free hard alloys TiC–Ni is a popular direction in the field of the development of protective coatings [3–6]. Carbide grains in such materials provide high hardness and wear resistance, while the nickel matrix increases strength and corrosion resistance [7, 8]. When processing steel by TiC–Ni electrodes, titanium carbide and solid solution of nickel in iron are formed in the coating, which leads to the formation of a continuous

coating without microcracks and macrocracks [4]. It should be noted that alloying steel with nickel leads to an increase in its hardness, strength, and plasticity [9, 10]. The additional introduction of chromium into a metallic binder increases mechanical and tribological properties, as well as the fire resistance of ESA coatings [5]. The introduction of ZrO₂, Al₂O₃, NbC, WC, etc., additives into the composition of TiC–Ni and TiC–NiCr electrodes makes it possible to increase the growth rate of coatings by 40–80% and increase microhardness by almost 40% [11], fire resistance by 25%, and decrease the friction coefficient almost twofold [6]. Coating alloying by rare-earth metals and their oxides affects gas discharge running, increases the coating hardness by 30% [12] and fracture toughness by 35% [13], corrosion resistance more than by 80%, and lowers the friction coefficient by 30% [14].

We previously found [15] that the introduction of 1 at % Eu₂O₃ into the composition of the TiC–NiCr electrode positively affects the gas discharge charac-

teristics and increases the growth rate of the coating. In addition to the influence on the regularity of gas discharge burning, europium oxide improves mechanical and strength properties of electrode materials [16]. This study is focused on a detailed investigation into the structure and properties of coatings deposited on substrates made of steel 40Kh by electrospark alloying applying TiC–NiCr and TiC–NiCr–Eu₂O₃ electrodes.

EXPERIMENTAL

Powders of titanium carbide—85.9 wt % (81 wt %), nickel—5.4 wt % (5.1 wt %), chromium—8.7 wt % (8.2 wt %), and europium oxide (5.7 wt %) were used as the initial components for the fabrication of electrodes. The powders were mixed in an Aktivator-2S planetary centrifugal mill (ZAO Aktivator, Novosibirsk) in argon for 5 min. The compaction was performed using a hydraulic press at a pressure of 7.5 MPa. Compacted briquettes were sintered in the Al₂O₃ pouring using a VE-3-16 vacuum furnace (OOO NPP VakETO, Moscow) at 1450°C for 60 min. TiC–NiCr and TiC–NiCr–Eu₂O₃ electrodes 4 × 4 × 50 mm in size were formed. Polished discs made of steel 40Kh with a size of Ø30 × 5 mm were used as the substrates. The substrates were ultrasonically cleaned in isopropanol for 5 min before coating deposition using an UZDN-2T installation (NPP UkrRosPribor, Sumy, Ukraine).

The ESA of coatings was performed in argon under a pressure of 10⁵ Pa applying an Alier-Metal 303 installation (SCINTI, Kishinev, Moldova) using the following treatment parameters: the current force was 120 A, the voltage was 20 V, the pulse duration was 20 μs, the frequency was 640 Hz, the duty factor was 1.3%, and the deposition time was 30 min. Coatings were deposited in two modes, notably, with direct polarity (DP), when the electrode plays the role of the anode, and reversed polarity (RP), when the electrode is the cathode.

The morphology and the elemental and phase compositions of electrodes and coatings were determined by scanning electron microscopy (SEM) and energy dispersive spectroscopy (EDS) using an S-3400N microscope (Hitachi High-Technology Corp., United States) with the Noran 7 attachment (Thermo Scientific, United States) and by X-ray diffraction (XRD) using an AXS D8 Advance device (Bruker, Germany) using CuK_α radiation. The Vickers hardness of electrodes was established using an HVS-50 digital hardness meter (Time Group Inc., China) under a load of 5 kg. The mechanical properties of coatings such as hardness, Young modulus, and elastic recovery were studied using a Nano-Hardness Tester meter (CSM Instruments, Switzerland) equipped with a Berkovich indenter under a load of 4 mN. Tribological testing on determining the friction

coefficient was performed using a high-temperature tribometer (CSM Instruments, Switzerland) according to the pin–disc scheme. The samples were tested in contact with the Al₂O₃ little ball 6 mm in diameter under the following conditions: $t = 23$ and 500°C, linear velocity 10 cm/s, and normal load 5 N. To investigate the wear tracks and determine the roughness of electrospark coatings, we used a WYKO NT 1100 optical profilometer (Veeco Instruments Inc., United States). The abrasive resistance of the samples was evaluated using a Calowear tester (NIITavtoprom, Moscow) [17] under a load of 10 N and revolution rate of 153 and 247 rpm. A 100Cr6 steel little ball 27 mm in diameter was used as a counterbody. The suspension containing diamond particles 15 μm in size was deposited on the sample surface before testing. The testing duration was 5 min. The impact testing was performed using an Impact Tester device (CemeCon, Germany, Greece). During the impact testing, the counterbody 5 mm in diameter periodically penetrates into the sample surface under the effect of the established load. The plastic deformation stage appears in the loading instant, due to which the region of indenter contacting with the surface does not recover its initial plane shape forming herewith the constant imprint (crater). The technical parameters of the Impact Tester device are as follows:

Impact force, N	150–1300
Frequency, Hz	50
Indenter diameter, mm	5
Cycle duration for 1 million impacts, h	5.5
Process control	Computer controlling
Software	ITControl (CemeCon)

The Impact Tester device consists of piston 1, on which counterbody holder 2 is fastened, two-position stage 3 for the establishment of samples, mobile block 4, piezoelectric detector 5, system of sample air-cooling (Fig. 1), and computer controlling module.

This module consists of a personal computer equipped with a proportional-integral and differential controller for installation controlling. The ITEC software makes it possible to determine the fatigue coating properties in the form of the Smith and Wheeler diagrams in the case of the computer simulation by the finite element method of the perpendicular impact testing process. The testing mode is specified using the ITControl software (CemeCon) of the device by varying two main characteristics—the impact force and number of impacts.

The operational principle of the device is based on the impact (single or cyclic) effect on the surface under study by the indenter (the ball) with fixed load and frequency. The alternate voltage with a frequency of 50 Hz is supplied to the mobile block during testing.

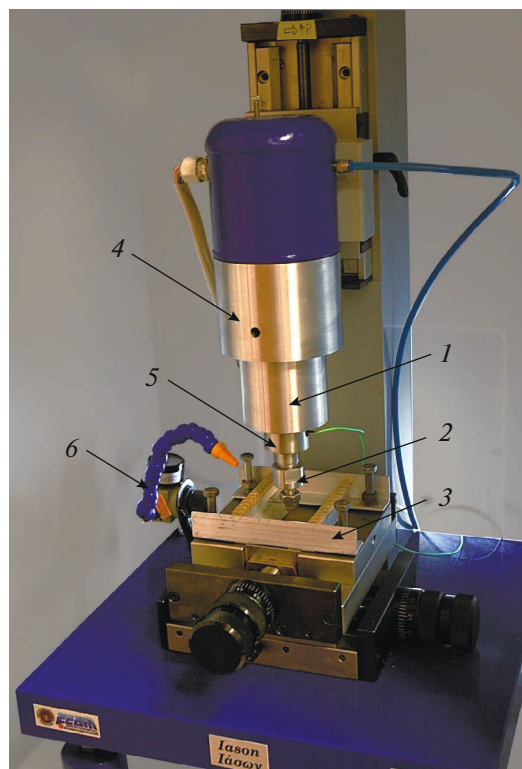


Fig. 1. Appearance of the Impact Tester installation. (1) Piston, (2) counterbody holder, (3) stage for sample establishment, (4) mobile block, (5) piezosensor, and (6) air duct.

When moving the entire block along the vertical axis, the necessary maximal load is established, which is monitored using a piezosensor, due to which oscillatory motions in the vertical plane with amplitude of 1 mm appear. When touching the sample surface, the mechanical oscillations transform into the pulse load; i.e., the kinetic energy transforms into the deformation energy.

Using this device, we can evaluate the following characteristics: the wear rate under the conditions of impact effects, adhesion and cohesion strength of coatings, and material fatigue strength and crack resistance [18, 19]. A cycle of impacts with a constant frequency of 50 Hz was performed for the coatings under study using a little ball 5 mm in diameter made of the WC–Co hard alloy. Each sample was subjected to tests consisting of 100 000 impacts under dry air conditions at an applied load of 1200 N.

To determine the wear parameters, we used a WYKO NT 1100 optical profilometer. The electrochemical properties of coatings were evaluated using a three-electrode cell with the VoltaLab 50 potentiostat (Radiometer Analytical, France). Testing was performed in the 1N H₂SO₄ solution using the Ag/AgCl reference electrode and auxiliary Pt electrode. All potentials were recalculated relative to the standard

hydrogen electrode. The corrosion current density (i_{cor}) was calculated using the Tafel formula. The oxidation of coatings was studied at humidity <30%. The coatings were charged into a preliminary heated SNOL 7.2/1200 furnace (Umega, Lithuania) and annealed in air at $t = 400, 500, 600, 700,$ and 800°C with isothermal holding for 1 h at each temperature. Annealed samples of coatings deposited under the DP were studied using a Profiler-2 glow-discharge optical emission spectrometer (GDOES) (HORIBA Jobin Yvon, France). Coatings deposited in the RP mode were not measured because of their large roughness. The oxidation kinetics of coatings was investigated by the gravimetric method using a KERN 770 analytical balance (Germany) after annealing for 10, 30, 60, and 180 min at each temperature. The oxidation index (Δm_s) was determined according to the procedure described in [20].

RESULTS AND DISCUSSION

Structure and Properties of Electrodes

The results found using the EDS method showed that electrode 1 has the following composition, wt %: Ti 71.0, C 19.0, Ni 2.9, Cr 7.1, while electrode 2 has the following composition: Ti 69.5, C 15.6, Ni 2.5, Cr 6.9, and Eu₂O₃ 5.7. According to the XRD data (Fig. 2), it is seen that TiC grains, a solid solution of nickel and chromium NiCr, and europium in the form of Eu₂O₃ oxide are present in electrodes.

Numerous peaks correspond to planes (111), (200), (311), (222), (400), (311), and (420) of the titanium carbide-based fcc phase. The peaks of the NiCr solid solution observed at angles $2\theta = 43.8^{\circ}, 50.8^{\circ},$ and 72.6° , and Eu₂O₃ peaks at $2\theta = 24.8^{\circ}$ and 30° are also present in the case of electrode 2. The titanium carbide crystallite sizes were found using the Scherrer formula. The results showed that their values, determined from the broadening of lines (111), (200), and (311), are 45, 46, and 35 nm, respectively. The TiC crystallite sizes for other lines were in a range of 18–27 nm. The sizes for peaks corresponding to Eu₂O₃ were 44 nm (at $2\theta = 24.8^{\circ}$) and 22 nm (at $2\theta = 30^{\circ}$).

The SEM images of electrodes (Fig. 3) confirm the results found by the XRD method. It is seen that the TiC grains and interlayers of the solid solution of nickel and chromium are present in the composition of electrodes 1 and 2. The Eu₂O₃ grains (bright segments in SEM images) are observed in the case of the doped electrode.

According to our data found using the hardness meter, europium oxide affects the mechanical properties of electrodes. The hardness of electrode 2 (18–20 GPa) is 25% higher than the values for the electrode without the Eu₂O₃ addition (14–16 GPa). An analysis of the published data shows that the TiC–Ni electrode formed by the SHS method has hardness

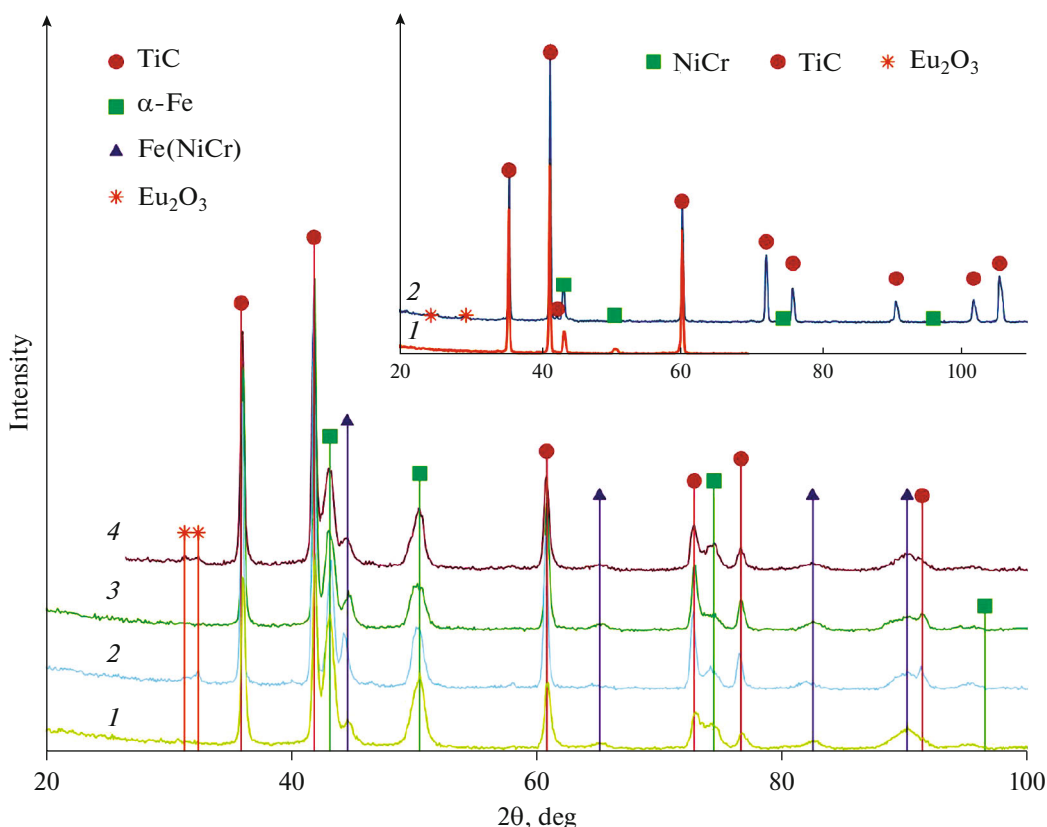


Fig. 2. X-ray diffraction patterns of coatings 1–4. X-ray diffraction patterns of TiC–NiCr (1) and TiC–NiCr–Eu₂O₃ (2) electrodes are shown in insert.

13.8 GPa. Various additives (ZrO₂, Al₂O₃, NbC, etc.) to the base composition allow us to increase the hardness characteristics to 16.9 GPa [21]. The introduction of Mo into the composition of the TiC–Ni electrode ($H = 13$ GPa) increases its hardness by 30% [22].

Elemental Analysis of Coatings

Elemental compositions of ESA coatings on samples 1–4 fabricated using TiC–NiCr and TiC–NiCr–Eu₂O₃ electrodes under the DP and RP are presented in Table 1.

Contents of Ti, C, Ni, and Cr for coatings 1 and 2 differed by 2.7, 0.3, 0.7, and 0.1 wt %, respectively. The Eu₂O₃ addition had led to a regular decrease in the concentration of other electrode elements; however,

the ratio between them remained invariable. The content of the main substrate component—Fe—upon the passage from coating 1 to coating 2 decreased by 22%, which can be explained by the larger thickness of coating 2 with the Eu₂O₃ additive. The difference in the substrate component (Fe) content for coatings 3 and 4 was 12%.

The GDOES analysis showed that a clearly pronounced concentration gradient is present in coatings. The signal from Fe increases monotonically from the coating surface to the substrate, while the concentrations of electrode components decrease. Similar results are typical of the coatings prepared by the ESA method. The GDOES results confirmed the presence of Eu in coatings formed using the TiC–NiCr–Eu₂O₃ electrode.

Table 1. Composition (wt %) and properties of coatings 1–4

Sample	Coating	Mode	Ti	C	Ni	Cr	Eu	Fe	H , GPa	E , GPa	W , %	f
1	TiC–NiCr	DP	31.7	11.3	3.6	6.8	–	47.3	23.7	252	66	0.33
2	TiC–NiCr–Eu ₂ O ₃	DP	34.4	11.0	4.3	6.9	6.5	36.9	20.8	230	62	0.36
3	TiC–NiCr	RP	36.7	14.2	3.6	5.5	–	40.0	26.5	333	62	0.30
4	TiC–NiCr–Eu ₂ O ₃	RP	33.9	11.9	3.1	4.9	11.9	35.2	18.9	285	55	0.34

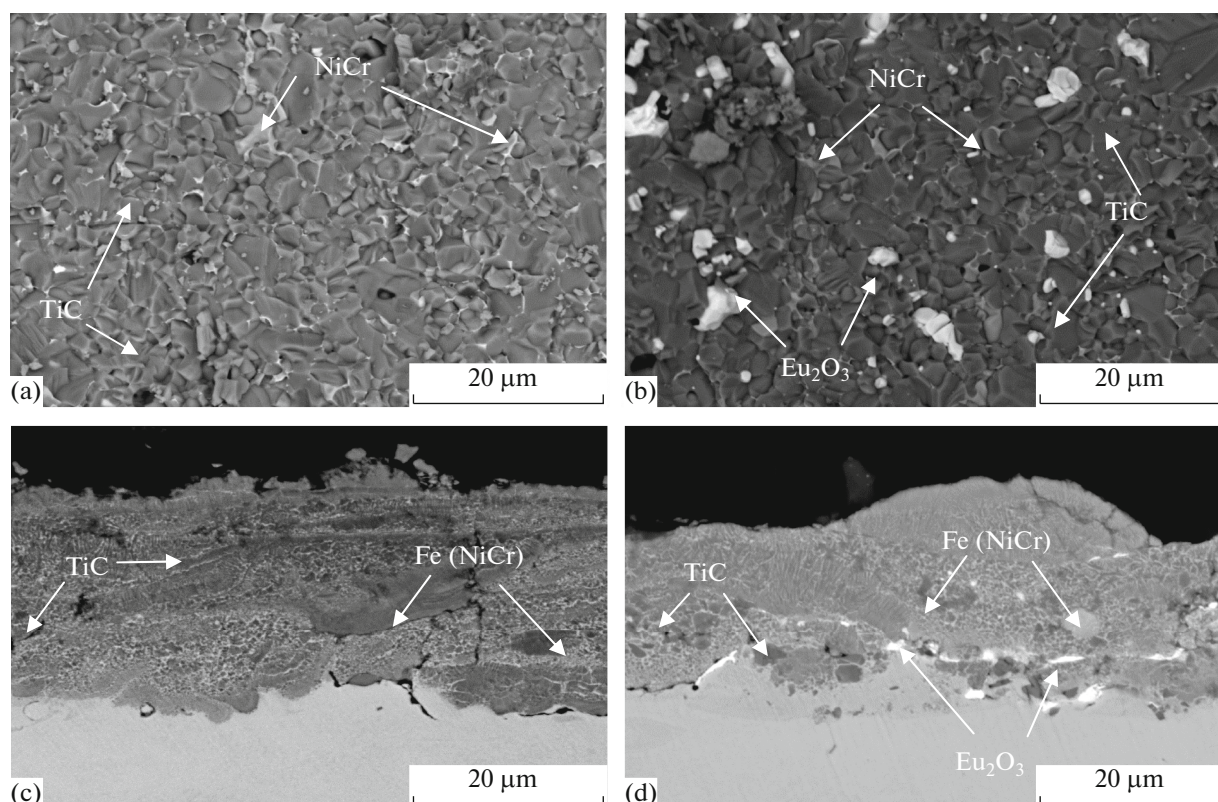


Fig. 3. Microphotographs (SEM) of (a) TiC–NiCr and (b) TiC–NiCr–Eu₂O₃ electrodes and transverse metallographic sections (c) 3 and (d) 4.

Microstructure and Phase Composition of Coatings

Figure 2 shows X-ray diffraction patterns of coatings 1–4. The peaks associated with reflections from planes (111), (200), (220), (311), and (222) of the titanium carbide-based fcc phase are found for all coatings. It is established that the peaks corresponding to planes (110) and (211) belong to the α -Fe phase. The peaks in positions $2\theta = 31.4$ and 32.4° characteristic of Eu₂O₃ are revealed in X-ray diffraction patterns in the case of coatings 2 and 4 formed using the doped electrode [23, 24].

The size of titanium carbide crystallites, determined from the broadening of lines (111) for coatings 1–4, is identical, being 22 nm. Calculations for the strongest line (200) showed that, when passing from coating 1 to coating 2, the size of TiC crystallites remained invariable, being 30 nm, while for line (220), it decreased from 25 to 20 nm. The size of TiC crystallites for coatings 3 and 4 found from line (200) also decreased from 30 to 18 nm with the introduction of Eu₂O₃. We note that grain refining of the host phase is a characteristic feature of europium oxide [25]. The size of Eu₂O₃ grains for coatings 2 and 4 was ~ 20 nm.

The lattice constant of undoped coatings was in a range of 0.429–0.430 nm, while its values for coatings

with Eu₂O₃ differed insignificantly (0.430–0.431 nm) and were somewhat lower than for bulk TiC (0.433 nm). A decrease in the lattice parameter can be explained by the presence of tensile stresses [26] or by the deviation of the composition of the TiC phase from stoichiometry [27].

It is seen in photographs of transverse metallurgical sections of coatings (Fig. 3) that titanium carbide grains and interlayers of the NiCr solid solution in Fe are present in their composition and the Eu₂O₃ grains are additionally present in the case of coatings 2 and 4. It should be noted that europium oxide is situated both at the coating interface with the substrate and in the coating bulk. The TiC grain size evaluated by microphotographs was from 10 to 70 nm. No substantial structural distinctions were found for coatings formed at various types of polarity. The composition of TiC and Eu₂O₃ phases was close to stoichiometric according to the EDS data. The Ni and Cr contents in the iron-based solid solution were of about 20 and 25%, respectively.

It was established that the roughness of coatings is mainly affected by polarity. Roughness parameter R_a for coatings 1 and 2 was 2.95 μm , and it was 5.10 and 5.98 μm for coatings 3 and 4, respectively. When passing from the DP to RP, the coating roughness

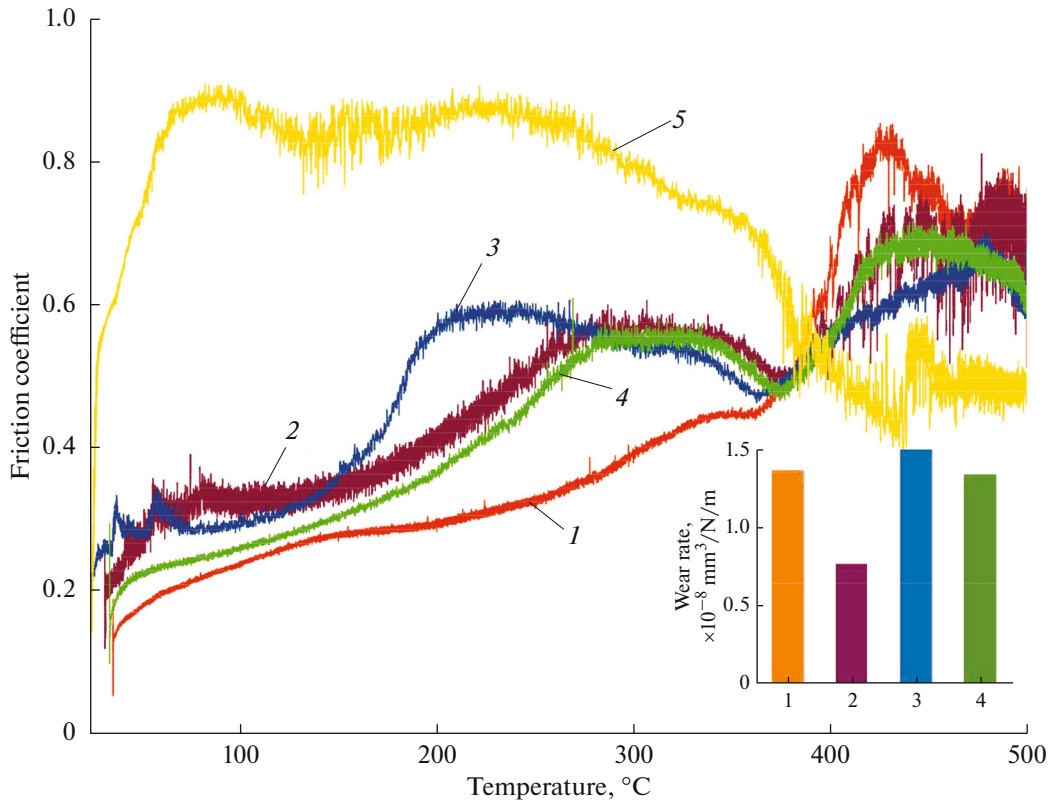


Fig. 4. Friction coefficient of coatings 1–4 and substrate 5 depending on temperature. The wear rate of coatings 1–4 is shown in insert.

increases by a factor of 1.7–2.7. The Eu_2O_3 addition affects the coating roughness more weakly.

Mechanical Properties of Coatings

Sample testing by nanoindentation was performed for transverse metallurgical sections of coatings. Coating 1 had hardness $H = 23.7$ GPa, the Young modulus $E = 252$ GPa, and elastic recovery $W = 66\%$ (Table 1). When introducing the additive, these characteristics for coating 2 became 6–12% lower and were $H = 20.8$ GPa, $E = 230$ GPa, and $W = 62\%$. Coating 3 had the highest hardness (26.5 GPa) and elasticity modulus (333 GPa). Sample 4 had a low hardness and low elastic recovery of 55%. It is noteworthy that the coating hardness decreased by 12–28% due to the introduction of europium oxide into the electrode composition. However, the hardness of all ESA coatings exceeded the values found for the substrate made of steel 40Kh ($H = 11$ GPa) by more than a factor of 1.7. A decrease in E is associated with the presence of the substrate component in the coating composition. We note that the low Young modulus in combination with high hardness can positively affect the wear resistance of coatings [28]. According to the published data, the ESA coatings prepared using the TiC–Ni electrodes have a hardness of 13.9 GPa [29]. When introducing

Cr into this composition, it increases to 15 GPa [5]. The coating hardness increases to 17 GPa after alloying the TiC–Ni base composition by various elements (such as Mo, Al_2O_3 , and ZrO_2) [29]. Thus, ESA coatings prepared in our work have the higher mechanical characteristics when compared with those studied previously.

Friction Coefficient and Wear Resistance of Coatings

According to the results of room-temperature tribological testing, coatings 1 and 2 had close initial friction coefficient (f) at a level of 0.2. The magnitude of f gradually increased throughout testing, reaching ~ 0.4 . Average values for coatings 1 and 2 were 0.33 and 0.36, respectively (Table 1). Coating 3 had the lowest and stable $f \sim 0.30$. The friction coefficient of coating 4 was 0.30 up to a distance of 100 m, after which its average value increased to 0.34. No wear of coatings 1–4 was found for a distance of 200 m.

The results of high-temperature tribological tests in the form of temperature dependences of the friction coefficient are shown in Fig. 4.

Curves $f(t)$ for all coatings were similar, notably, the magnitude of f gradually increases in a temperature range from 28–35 to 380°C, while the inflection point

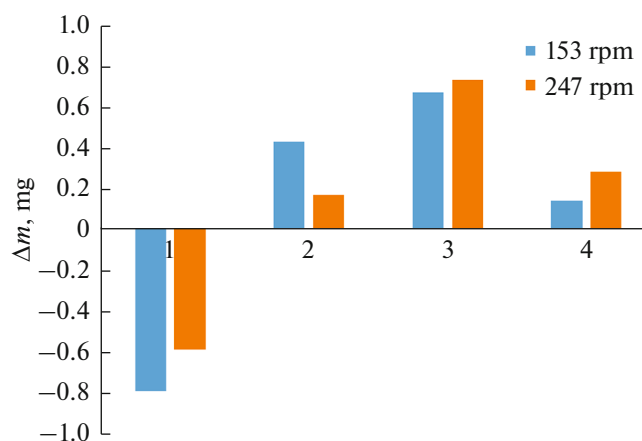


Fig. 5. Abrasive wear of coatings 1–4.

observed at $t = 400^\circ\text{C}$ evidences carbon burning out from the surface of coatings [30], due to which the friction coefficient increases abruptly. Coating 1 had low $f = 0.30$ up to $t = 380^\circ\text{C}$. The friction coefficient fell by 12% upon the passage from coating 3 to doped coating 4. A decrease in f for a steel substrate after $t = 300^\circ\text{C}$ occurs due to the formation of iron oxides in the tribocontact zone, which can exert the lubricating effect [31]. All coatings can be successfully applied to improve the tribological properties of steel at temperatures up to 400°C .

An analysis of wear tracks after high-temperature testing showed that the wear traces of the coating surface are difficult to find using an optical and electron microscope because of their high roughness ($R_a = 2\text{--}6\ \mu\text{m}$). Nevertheless, the wear rate was evaluated using calculations by profilograms found using an optical contactless profilometer. The wear rate of coatings 1, 3, and 4 differs insignificantly, being $V = (1.3\text{--}1.5) \times 10^{-8}\ \text{mm}^3/\text{N}/\text{m}$. Sample 2 has the highest wear resistance ($0.8 \times 10^{-8}\ \text{mm}^3/\text{N}/\text{m}$) at the minimal roughness ($R_a = 2.2\ \mu\text{m}$). Despite the fact that the europium oxide addition does not affect the room-temperature tribological properties of coatings, the sample with Eu_2O_3 showed the best wear resistance in high-temperature testing.

Table 2. Diameter (D) and depth (h) of craters

Sample	Coating	Mode	1200 N	
			$D, \mu\text{m}$	$h, \mu\text{m}$
1	TiC–NiCr	DP	800	27.5
2	TiC–NiCr– Eu_2O_3	DP	760	14.0
3	TiC–NiCr	RP	1030	22.5
4	TiC–NiCr– Eu_2O_3	RP	790	17.5

Abrasive-Wear Resistance of Coatings

Figure 5 shows the results of the abrasive-wear testing of coatings for various counterbody revolution rates. Coating 1 showed a decrease in the weight at $V = 153\ \text{rpm}$, which is directly conditioned by the coating wear.

The partial pickup of wear products was observed with an increase in the counterbody revolution rate to 247 rpm. An increase in the weight was characteristic of coatings 2–4, which can be associated with the coating roughness level and presence of microcracks and pores [32, 33]. Coating 2 had the smallest wear, with a little-ball revolution rate of 247 rpm. At the same time, coating 4 had the best wear resistance at $V = 153\ \text{rpm}$. Coatings 2 and 4, prepared using the doped electrode, had the best abrasive-wear resistance.

Cyclic Impact Load Resistance of Coatings

Geometric parameters of craters formed after impact dynamic testing and calculated based on 2D and 3D profiles (Fig. 6) are presented in Table 2.

The following crater sizes were characteristic of coating 1 after testing under an applied load of 1200 N: the diameter is $800\ \mu\text{m}$ and the depth is $27.5\ \mu\text{m}$ (Fig. 6).

Coating 2 with the Eu_2O_3 additive had the smallest crater depth ($h = 14\ \mu\text{m}$). Sample 3 had a larger crater diameter after the impact but a smaller depth when compared with the sample of the same composition formed under the DP. The crater depth for coating 4 is 22% smaller than that for sample 3. The results showed that the coatings prepared when applying the TiC–NiCr– Eu_2O_3 electrode had the higher impact resistance, while the crater depth did not exceed the coating thickness. We note that electrospark TiCNi coatings were previously studied. The crater depth after testing at a load of 1500 N was of about $40\ \mu\text{m}$ in this case [34].

Electrochemical Properties of Coatings

The results of the electrochemical analysis (corrosion potential ϕ and corrosion current density i_{cor}) are presented in Table 3.

Corrosion potentials of all coatings deposited on a steel substrate correspond to the free iron corrosion potential (190 V). This is associated with the fact that the electrolyte reaches the substrate through the cracks and coating defects, and the abundant dissolution of iron occurs.

The corrosion current density for all coatings was determined by polarization curves (Fig. 7).

The magnitude of i_{cor} for coating 1 was $0.84\ \text{mA}/\text{cm}^2$, which is larger than the corrosion current density for coating 2 ($0.49\ \text{mA}/\text{cm}^2$). This characteristic for coating 3 ($4.2\ \text{mA}/\text{cm}^2$) corresponded to the corrosion current density of iron ($4.5\ \text{mA}/\text{cm}^2$).

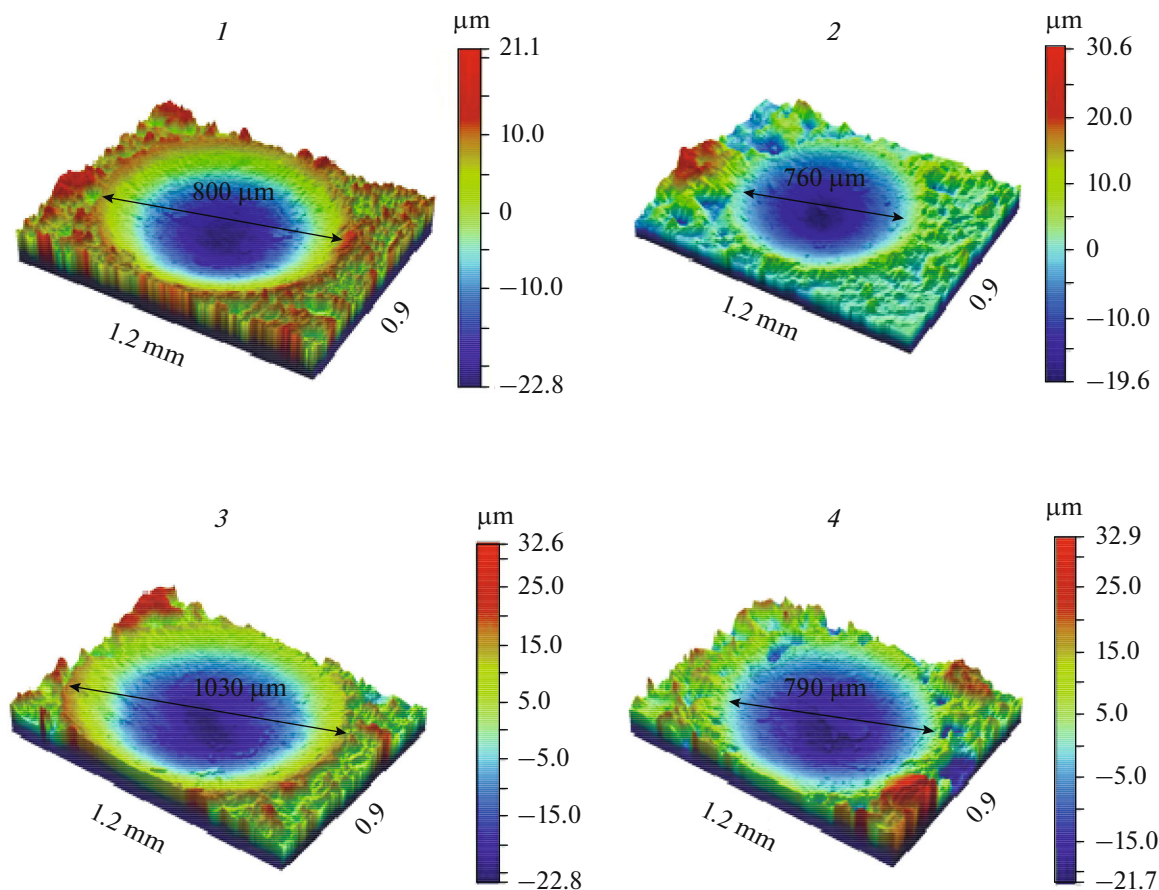


Fig. 6. 3D profiles of craters resulting from the impact testing of samples 1–4.

Coating 4 had the lowest corrosion current density (0.19 mA/cm^2). This can be associated both with its larger thickness and with the positive role of the REM additive [35, 36], the concentration of which is maximal in this coating.

Fire Resistance of Coatings

A widespread method for evaluating fire resistance is the investigation into the oxidation kinetics [37, 38]. However, C, B, and N, which form volatile compounds with oxygen, can burn out during the oxidation. Therefore, we investigated fire resistance by two methods, notably, by the variation in weight and by the variation in oxygen and carbon concentration in coatings determined from elemental profiles of annealed coatings.

The experiments performed at $t = 400^\circ\text{C}$ did not allow us to reveal the oxidation mechanism because of small values ($<0.2 \text{ g/m}^2$) and large spread of Δm_S in the case of coatings 2 and 4 with the Eu_2O_3 additive. Coatings 1 and 3 (without the additive), after protective oxide formed on the surface [39] for the first 10–30 min, were not oxidized further. The analysis of the

kinetic dependences of oxidation of the samples at $t = 500, 600, \text{ and } 700^\circ\text{C}$ allowed us to establish that oxidation proceeds according to the law close to linear in all cases (coatings 1–4). The data on characteristics of oxidation determined from kinetic curves (Fig. 8) are shown in Table 1.

It is seen that the Eu_2O_3 addition decreases the values of this characteristic (Δm_S) at $t = 500$ and 600°C by 10–13%, and the positive effect is stronger for coatings formed under the direct polarity. The minimal oxida-

Table 3. Electrochemical and gas corrosion of coatings and substrate

Sample	ϕ , mV	I_{cor} , mA/cm^2	Δm_S , g/m^2 , at t , $^\circ\text{C}$		
			500	600	700
1	179	0.84	1.162	1.211	2.289
2	178	0.49	1.031	1.062	2.938
3	174	4.2	1.484	1.531	3.741
4	182	0.19	1.337	1.373	1.926

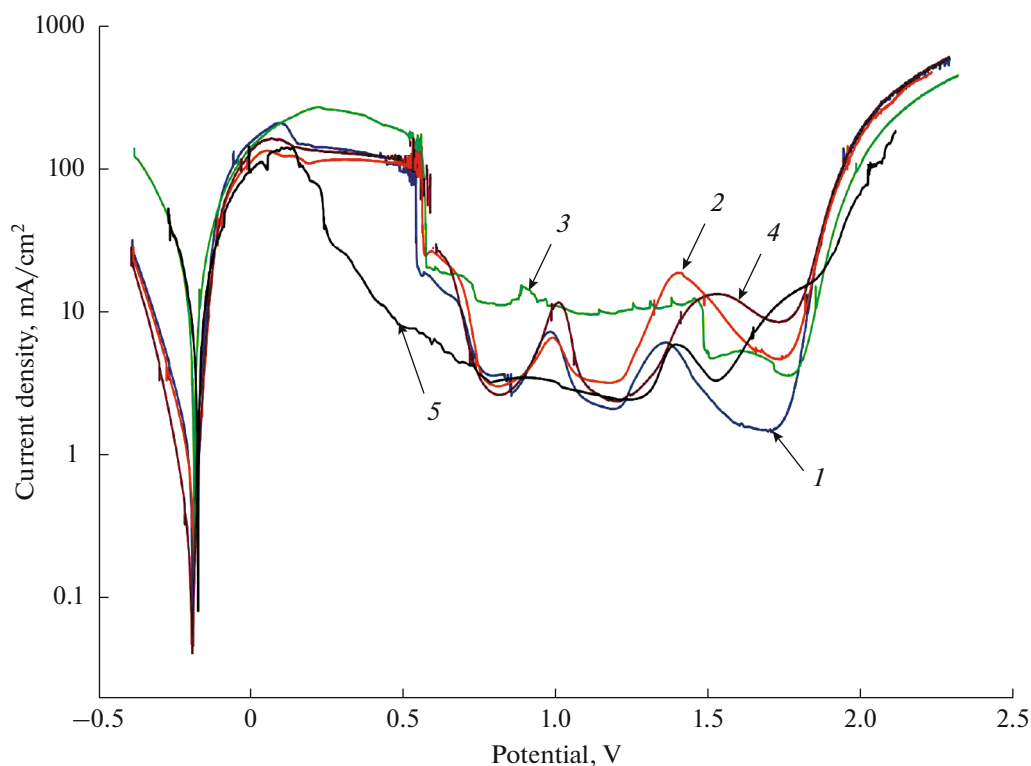


Fig. 7. Polarization curves of coatings 1–4 and substrate 5.

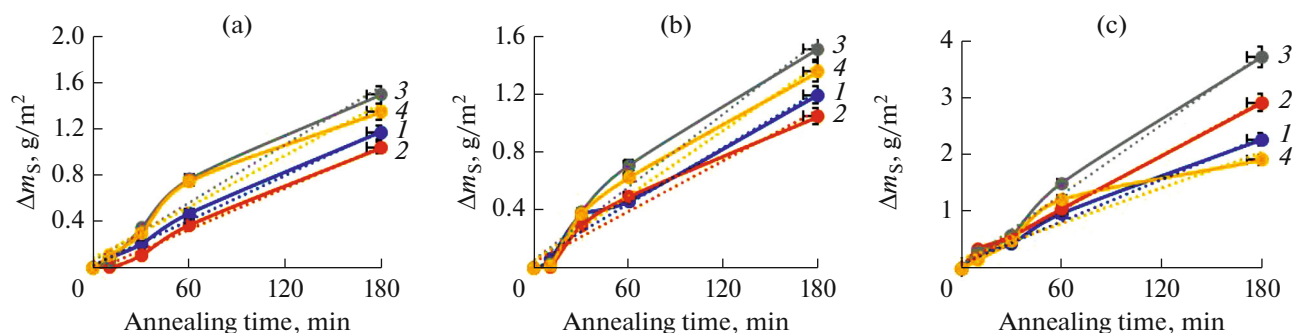


Fig. 8. Dependence of the oxidation index of samples 1–4 on the annealing time at $t =$ (a) 500, (b) 600, and (c) 700°C. Curves plotted by the assumption of the linear character of dependences are marked by the dotted lines.

tion characteristic (1.926 g/m^2) at $t = 700^\circ\text{C}$ was inherent to coating 4 with the Eu_2O_3 addition.

The oxidation depth of coatings was determined by the GDOES data. The penetration depth of oxygen for samples 1 and 2 after annealing at $t = 500^\circ\text{C}$ was in the limits of 5–6 μm , while the Eu_2O_3 addition at $t = 600$ and 700°C led to a 20% decrease in the oxidation depth. Thus, the Eu_2O_3 -containing coatings showed higher fire resistance than coatings without the addition in both types of testing, and the positive effect largely manifested itself at higher temperatures. This

can be associated with the ability of REMs to stabilize the oxide phase [40].

CONCLUSIONS

The coatings on the 40Kh steel substrate were formed by the ESA method using TiC–NiCr and TiC–NiCr– Eu_2O_3 electrodes in the direct and reversed polarity modes. The coatings contained phases of titanium carbide, a solid solution of nickel and chromium in iron, and europium oxide (when using the TiC–NiCr– Eu_2O_3 electrode).

The addition of europium oxide into the TiC–NiCr electrode material promoted a 25% increase in its hardness and strength.

The introduction of Eu_2O_3 led to a decrease in the coating hardness from 23–27 to 18–20 GPa and exerted no noticeable effect on the friction coefficient in a broad temperature range ($t = 20\text{--}500^\circ\text{C}$); however, a 20% increase in the cyclic impact resistance and 60% increase in the abrasive wear, a 50% increase in fire resistance, and 95% increase in the corrosion resistance of coatings were observed.

ACKNOWLEDGMENTS

The investigations into the abrasive effect and impact resistance, as well as tribological testing at elevated temperatures, are supported by the Russian Scientific Foundation, project no. 15-19-00203-Π. We thank A.N. Sheveiko and N.V. Shvyndina for help in electrochemical and structural studies of coatings.

CONFLICT OF INTEREST

The authors declare that they have no conflict of interest.

REFERENCES

- Kumar, S., Singh, R., Singh, T.P., and Sethi, B.L., Surface modification by electrical discharge machining: A review, *J. Mater. Proc. Technol.*, 2009, vol. 209, pp. 3675–3687.
- Chen, Z. and Zhou, Y., Surface modification of resistance welding electrode by electro-spark deposited composite coatings. Pt. I. Coating characterization, *Surf. Coat. Technol.*, 2006, vol. 201, pp. 1503–1510.
- Nikolenko, S.V., Verkhoturov, A.D., Syui, N.A., and Kuz'michev, E.N., Influence of electrospark discharge parameters on roughness and microabrasive wear of steel 45 surface after ESA by TiC-based electrodes, *Surf. Eng. Appl. Electrochem.*, 2016, vol. 52, pp. 342–349.
- Panteleenko, F.I., Sarantsev, V.V., Stolin, A.M., Bazhin, P.M., and Azarenko, E.L., Formation of composite coatings based on titanium carbide via electrospark alloying, *Surf. Eng. Appl. Electrochem.*, 2011, vol. 47, pp. 336–348.
- Andreev, A.V., Litovchenko, I.Y., Korotaev, A.D., and Borisov, D.P., Thermal stability of Ti–C–Ni–Cr and Ti–C–Ni–Cr–Al–Si nanocomposite coatings, *J. Phys. Conf. Ser.*, 2015, vol. 652, paper 012057.
- Levashov, E.A., Kudryashov, A.E., Vakaev, P.V., Malochkin, O.V., Gammel, F., Suchentrunk, R., and Moore, J.J., The prospect of nanodispersive powders application in surface technologies, *Surf. Coat. Technol.*, 2004, vol. 180–181, pp. 347–351.
- Rajabi, A., Ghazali, M.J., Syarif, J., and Daud, A.R., Development and application of tool wear: A review of the characterization of TiC-based cermets with different binders, *Chem. Eng. J.*, 2014, vol. 255, pp. 445–452.
- Zohari, S., Sadeghian, Z., Lotfi, B., and Broeckmann, Ch., Application of spark plasma sintering (SPS) for the fabrication of in situ Ni-TiC nanocomposite clad layer, *J. Alloys Compd.*, 2015, vol. 633, pp. 479–483.
- Hosseini Far, A.R., Mousavi Anijdan, S.H., and Abbasi, S.M., The effect of increasing Cu and Ni on a significant enhancement of mechanical properties of high strength low alloy, low carbon steels of HSLA-100 type, *Mater. Sci. Eng. A*, 2019, vol. 746, pp. 384–393.
- Baron, C. and Springer, H., On the effect of Ni additions to Fe–Cr–B high modulus steels, *Mater. Des.*, 2019, vol. 167, paper 107624.
- Levashov, E.A., Malochkin, O.V., Kudryashov, A.E., Suchentrunk, R., and Gammel, F., Effect of nanosized powders on the structure and properties of electrospark alloyed coatings, *J. Mater. Synth. Proc.*, 2001, vol. 9, no. 4, pp. 199–206.
- Fang, Y., Cui, X., Cai, Z., Wang, C., and Jin, G., Influence of La_2O_3 addition on nano indentation hardness and residual stress of Stellite 6 coating prepared by plasma cladding, *J. Rare Earth*, 2018, vol. 36, pp. 873–878.
- Li, J., Wang, H.P., Li, M.P., and Yu, Z.S., Effect of yttrium on microstructure and mechanical properties of laser clad coatings reinforced by in situ synthesized TiB and TiC, *J. Rare Earth*, 2018, vol. 29, pp. 477–483.
- Zhu, R., Li, Z., Li, X., and Sun, Q., Microstructure and properties of the low-power-laser clad coatings on magnesium alloy with different amount of rare earth addition, *Appl. Surf. Sci.*, 2015, vol. 353, pp. 405–413.
- Kiryukhantsev-Korneev, Ph.V., Levashov, E.A., and Shtansky, D.V., The effect of Eu_2O_3 additive to the TiCNiCr electrode on the formation of electrospark coatings, *Tech. Phys. Lett.*, 2018, vol. 44, pp. 753–755.
- Kiryukhantsev-Korneev, Ph., Sytchenko, A., Sheveyko, A., and Vorotilo, S., Deposited by pulsed cathodic arc evaporation in Ar, N_2 , and C_2H_4 environments using the TiC–NiCr– Eu_2O_3 cathode, *Coatings*, 2019, vol. 9, paper 230.
- Kiryukhantsev-Korneev, Ph.V., Phiri, J., Gladkov, V.I., Ratnikov, S.N., Yakovlev, M.G., and Levashov, E.A., Erosion and abrasion resistance, mechanical properties and structure of the TiN, Ti–Cr–Al–N, and Cr–Al–Ti–N coatings deposited by CFUBMS, *Protection of metals and physical chemistry of surfaces*, 2019, vol. 55, pp. 913–923.
- Bouzakis, K.-D., Vidakis, N., and David, K., The concept of an advanced impact tester supported by evaluation software for the fatigue strength characterization of hard layered media, *Thin Solid Films*, 1999, vols. 355–356, pp. 322–329.
- Bouzakis, K.-D., Maliaris, G., and Makrimalakis, S., Strain rate effect on the fatigue failure of thin PVD coatings: An investigation by a novel impact tester with adjustable repetitive force, *Int. J. Fatigue*, 2012, vol. 44, pp. 89–97.
- Bose, S., *High Temperature Coatings*, Amsterdam: Elsevier, 2018.
- Levashov, E.A., Mishina, E.S., Malochkin, O.V., Shtansky, D.V., Moore, J.J., and Fadeev, M.I., Structure and properties of dispersion-strengthened-with-nanosized particles refractory hard material TiC–Ni alloy, *Sci. Technol. Adv. Mater.*, 2003, vol. 4, no. 3, pp. 221–228.

22. Fu, Z., Huey, J., Sai, K., Gajjala, R., and Koc, R., Sintering, mechanical, and oxidation properties of TiC–Ni–Mo cermets obtained from ultra-fine TiC powders, *J. Alloys Compd.*, 2018, vol. 751, pp. 316–323.
23. Ahlawat, R., Rani, N., and Goswami, B., Synthesis and characterizations of Eu_2O_3 nanocrystallites and its effect on optical properties of Eu^{3+} , Eu^{2+} : SiO_2 nanopowder, *J. Alloys Compd.*, 2018, vol. 743, pp. 126–135.
24. Niu, T., Zhang, P., and Zheng, G., Liu I., Deng J., Jin Y., Jiao Z., Sun X. Tuning the charge transition process of Eu_2O_3 nanorods by coupling with Ag nanoparticles for enhanced photocatalytic performance, *J. Environ. Chem. Eng.*, 2017, vol. 5, pp. 2930–2936.
25. Hui, Y., Zhao, S.M., and Xu, J.Y., Doping concentration of Eu^{3+} as a fluorescence probe for phase transformation of zirconia, *J. Rare Earths*, 2015, vol. 33, pp. 717–725.
26. Paustovskii, A.V. and Gubin, Yu.V., Stresses in coatings obtained by electro-spark alloying and laser processing (review), *Mater. Sci.*, 1997, vol. 33, pp. 770–776.
27. Chen, Z. and Zhou, Y., Surface modification of resistance welding electrode by electrospark deposited composite coatings: Pt. I. Coating characterization, *Surf. Coat. Technol.*, 2006, vol. 201, pp. 1503–1510.
28. Leyland, A. and Matthews, A., On the significance of the H/E ratio in wear control: a nanocomposite coating approach to optimised tribological behavior, *Wear*, 2000, vol. 246, pp. 1–11.
29. Levashov, E.A., Pogozhev, Yu.S., Kudryashov, A.E., Rupasov, S.I., and Levina, V.V., TiC–Ni-based composite materials dispersion-strengthened by nanoparticles for electrospark deposition, *Russ. J. Non-Ferrous Met.*, 2008, vol. 49, pp. 397–403.
30. Mu, Y., Liu, M., and Zhao, Y., Carbon doping to improve the high temperature tribological properties of VN coating, *Tribol. Int.*, 2016, vol. 97, pp. 327–336.
31. Hardell, L., Hernandez, S., Mozgovoy, S., Pelcastre, L., Courbon, C., and Prakasha, B., Effect of oxide layers and near surface transformations on friction and wear during tool steel and boron steel interaction at high temperatures, *Wear*, 2015, vols. 330–331, pp. 223–229.
32. Gheisari, R. and Polycarpou, A.A., Three-body abrasive wear of hard coatings: Effects of hardness and roughness, *Thin Solid Films*, 2018, vol. 666, pp. 66–75.
33. Bagde, P., Sapate, S.G., Khatirkar, R.K., and Vashishtha, N., Friction and abrasive wear behaviour of Al_2O_3 – 13TiO_2 and Al_2O_3 – 13TiO_2 + Ni graphite coatings, *Tribol. Int.*, 2018, vol. 121, pp. 353–372.
34. Kiryukhantsev-Korneev, Ph.V., Sheveyko, A.N., Shvindina, N.V., Levashov, E.A., and Shtansky, D.V., Comparative study of Ti–C–Ni–Al, Ti–C–Ni–Fe, and Ti–C–Ni–Al/Ti–C–Ni–Fe coatings produced by magnetron sputtering, electro-spark deposition, and a combined two-step process, *Ceram. Int.*, 2018, vol. 44, pp. 7637–7646.
35. Subbarao, E.C., *The Science and Technology of Rare Earth Materials*, New York: Academic, 1980.
36. Ozgurluk, Y., Doleker, K.M., Ahlatci, H., and Karaoglanli, A.C., Investigation of hot corrosion behavior of thermal barrier coating (TBC) systems with rare earth contents, *Arabian J. Geosci.*, 2018, vol. 11, paper 267.
37. Kiryukhantsev-Korneev, Ph.V., Iatsyuk, I.V., Shvindina, N.V., Levashov, E.A., and Shtansky, D.V., Comparative investigation of structure, mechanical properties, and oxidation resistance of Mo–Si–B and Mo–Al–Si–B coatings, *Corros. Sci.*, 2017, vol. 123, pp. 319–327.
38. Kiryukhantsev-Korneev, Ph.V., Kudryashov, A.E., and Levashov, E.A., Recent achievements on oxidation-resistant Cr–(Al)–Si–B, Mo–(Al)–Si–B, Zr–(Al)–Si–B coatings obtained by magnetron sputtering and pulsed electrospark deposition (Part 2), *Galvano-technik*, 2018, vol. 109 (5), pp. 1044–1050.
39. Lavrenko, V.A., Glebov, L.A., Pomitkin, A.P., Chuprina, V.G., and Protsenko, T.G., High-temperature oxidation of titanium carbide in oxygen, *Oxid. Met.*, 1975, vol. 9, pp. 171–179.
40. Navrotsky, A., Lee, W., Mielewczyk-Gryn, A., Ushakov, S.V., Anderko, A., Wu, H., and Riman, R.E., Thermodynamics of solid phases containing rare earth oxides, *J. Chem. Thermodyn.*, 2015, vol. 88, pp. 126–141.

Translated by N. Korovin